Astronomy & Astrophysics

Properties of the dense cores and filamentary structures in the Vela C molecular cloud⋆

Xue-Mei Li[1,2] , Guo-Yin Zhang[2] , Alexander Men'shchikov[3] , Jin-Zeng Li[2], Chang Zhang[2] , and Zhong-Zu Wu[1]

[1] College of Physics, Guizhou University, Guiyang 550025, PR China
[2] National Astronomical Observatories, Chinese Academy of Sciences, Beijing 100101, PR China
  e-mail: zgyin@nao.cas.cn; ljz@nao.cas.cn
[3] Université Paris-Saclay, Université Paris-Cité, CEA, CNRS, AIM, 91191 Gif-sur-Yvette, France
  e-mail: alexander.menshchikov@cea.fr

ABSTRACT

The initial and boundary conditions of the Galactic star formation in molecular clouds are not well understood. In an effort to shed new light on this long-standing problem, we measured the properties of dense cores and filamentary structures in the Vela C molecular cloud, observed with *Herschel*. We used the hires algorithm to create high-resolution surface densities (11.7″) from the *Herschel* multiwavelength dust continuum. We applied the getsf extraction method to separate the components of sources and filaments from each other and their backgrounds before detecting, measuring, and cataloging the structures. The cores and filamentary structures constitute 40% of the total mass of Vela C; most of the material is in the low-density molecular background cloud. We selected 570 reliable cores, of which 149 are the protostellar cores and 421 are the starless cores. Almost 78% (329 of 421) of the starless cores were identified with the gravitationally bound prestellar cores. The exponent of the CMF ($\alpha = 1.35$) is identical to that of the Salpeter IMF. The high-resolution surface density image helped us determine and subtract backgrounds and measure the sizes of the structures. We selected 68 filaments with at least one side that appeared not blended with adjacent structures. The filament widths are in the range from 0.15 pc to 0.63 pc, and have a median value of $W = 0.3 \pm 0.11$ pc. The surface densities of filaments are well correlated with their contrasts and linear densities. Within uncertainties of the filament instability criterion, many filaments (39) may be both supercritical and subcritical. A large fraction of filaments (29), in which are found 94 prestellar cores, 83 protostellar cores, and only 1 unbound starless core, can definitely be considered supercritical. Taking into account the uncertainties, the supercritical filaments contain only prestellar and protostellar cores. Our findings support the idea that there is a direct relationship between the CMF and IMF and that filaments play a key role in the formation of prestellar cores, which is consistent with the previous *Herschel* results.

Key words. stars: formation – ISM: clouds – ISM: structure – submillimeter: ISM

1. Introduction

Star formation takes place within molecular clouds (André et al. 2014; Heyer & Dame 2015) that generally appear as blends of (round) sources, filamentary structures, large-scale background, and small-scale fluctuations. Separations of the structural components, measurements, and analyses of the sources and filaments are thought to improve our understanding of the initial conditions of star formation (cf. Bergin & Tafalla 2007; André et al. 2010).

Photometric surveys of the nearby ($\lesssim 500$ pc) molecular clouds and Galactic plane with *Herschel*, covering thermal far-IR and submillimeter continuum in five bands between 70 and 500 μm, probe the peak of the dust spectral energy distribution (SED), and allow the determination of the temperature and mass of the clouds (André et al. 2010; Molinari et al. 2010; Zhang et al. 2022). Multiband images from the *Herschel* telescope probe molecular clouds on a wide range of spatial scales. The orbital telescope has revolutionized our understanding of the link between the structure of the cold interstellar medium (ISM)

and the process of star formation. In particular, it has revealed filamentary structures with a wide range of sizes, densities, and morphologies that are indeed widespread in the molecular clouds (Men'shchikov et al. 2010; Li & Goldsmith 2012; Schisano et al. 2020). Most dense cores are located on the supercritical filaments, which suggests that the filaments can fragment into the cores that eventually collapse into stars (Könyves et al. 2015). The detailed fragmentation manner may be controlled by the linear density, geometrical bending, continued accretion of gas, and magnetic fields in the filaments (Zhang et al. 2020). The mass distribution of stars at their birth is known as the stellar initial mass function (IMF; Salpeter 1955; Kroupa 2001; Chabrier 2005; Kroupa et al. 2013). Since stars are born in dense cores, studies of the core mass function (CMF) might help understand the IMF (Andre et al. 2000; Ward-Thompson et al. 2007). A great deal of observational evidence supports the idea that CMFs are similar to the IMF in shape (e.g., Motte et al. 1998; Alves et al. 2007; Könyves et al. 2015). A mass conversion efficiency (from the cores to the stars) of approximately 1/3 was proposed by Alves et al. (2007).

The Vela molecular ridge (Galactic longitudes $l \approx 260$ to 275° and latitudes $b \approx \pm 3°$) was initially identified from low-resolution (5°) CO emissions in the direction of Vela, and roughly outlined as four molecular clouds named as Vela A, B,

---

C, and D (May et al. 1988; Murphy & May 1991). Vela A, C, and D have a kinematic distance of 0.7–1 kpc, whereas Vela B has a kinematic distance of 2 kpc (Murphy & May 1991). Vela C, the most massive of the four molecular clouds, spans roughly 3.5 degrees (south to north), and there are nest structures dispersed throughout a large amount of low-density gas in which low-mass stars form, and tight linear ridges in which massive or intermediate-mass stars form (Liseau et al. 1992; Lorenzetti et al. 1993; Yamaguchi et al. 1999; Massi et al. 2003; Baba et al. 2006; Netterfield et al. 2009; Hill et al. 2011). In previous studies (Molinari et al. 2011; Giannini et al. 2012; Minier et al. 2013; Massi et al. 2019), a distance of ∼700 pc to Vela C was adopted (Murphy & May 1991). The mean distance of Vela C, estimated by Zucker et al. (2020) from *Gaia* DR2 (Gaia Collaboration 2018) stellar parallaxes, is 905 ± 45 pc. The different distance measurements bring deviations of about 20% in the size and 60% in the mass of Vela C. Considering that *Gaia* measured distances with unprecedented precision, we adopted the distance of 905 pc in this work.

A decade ago, Giannini et al. (2012) detected dense cores in *Herschel* multiband images of Vela C with the CuTeX source extraction algorithm (Molinari et al. 2011), and Hill et al. (2011) traced skeletons of filaments with the DisPerSE algorithm (Sousbie 2011). For this work we chose to apply the multiscale source and filament extraction method getsf (Men'shchikov 2021a), which separates the structural components of sources, filamentary structures, and their backgrounds before applying a consistent approach to extracting both sources and filaments. The method has no free (unconstrained) parameters, which is a property that sets getsf apart from other extraction methods. Its single user-definable parameter, the maximum size of the sources or filaments of interest, is constrained from the observed images and is used to place a reasonable upper limit on the range of scales in a spatial decomposition of the observed images. Interested readers are referred to Men'shchikov (2021a) for a full description of getsf and to Men'shchikov (2021b) for its benchmarking that showed improved detection completeness and measurement accuracy with respect to the older getsources and getfilaments extraction methods (Men'shchikov et al. 2012; Men'shchikov 2013).

The outline of the present paper is as follows. In Sect. 2 we describe the *Herschel* submillimeter dust emission data. The data analysis and results are presented in Sect. 3. In Sect. 4 we discuss the extracted sources at different resolutions, their core mass function, and the filamentary structures. We summarize our conclusions in Sect. 5.

2. The *Herschel* images

The Vela C molecular cloud was observed on May 18, 2010, within the frame of the HOBYS imaging survey (PI: F. Motte, observation IDs: 1342196657, 1342196658; Motte et al. 2010). Using the PACS/SPIRE parallel mode (Poglitsch et al. 2010; Griffin et al. 2010) with a scanning speed of 20″ s^{-1}, an area of ∼1.4 × 3.2 deg^2 was imaged simultaneously at 70, 160, 250, 350, and 500 μm, with angular resolutions of 5.9, 11.7, 18.2, 24.9, and 36.3″, respectively. We retrieved the images from the *Herschel* Science Archive (HSA)[1]. The SPIRE extended-source calibrated map and PACS Unimap (Piazzo et al. 2015) products at level 2.5 were used, because the level 3 images did not undergo quality control at the *Herschel* Science Centre.

---

[1] http://archives.esac.esa.int/hsa/whsa/

3. Data analysis and results

3.1. The high-resolution surface density image

To properly compute the surface densities, it was necessary to derive zero-level offsets for the five *Herschel* images. We assume that the images probe the optically thin dust emission following the empirical fit (e.g., Planck Collaboration XI 2014),

$$I_\nu = \tau_{\nu_0} B_\nu(T) \left(\frac{\nu}{\nu_0}\right)^\beta, \tag{1}$$

where ν_0 is the reference frequency at which the optical depth τ_{ν_0} is estimated, I_ν is the specific intensity, and $B_\nu(T)$ is the Planck function for the emission of dust at temperature T and frequency ν. Using a modified blackbody fit to the *Planck* 353, 545, and 857 GHz images, and IRAS 100 μm data, Planck Collaboration XI (2014) presented all-sky maps of the dust optical depth at $\nu_0 = 353$ GHz (850 μm) and the dust temperature map with a resolution of 5′. Using $\beta = 2$, adopting $\nu_0 = 353$ GHz as the reference frequency, and substituting the optical depth at 353 GHz in Eq. (1), we used the *Planck* dust temperature map to derive the images at 70, 160, 250, 350, and 500 μm of Vela C, corresponding to the *Herschel* images. Convolving each *Herschel* image to the *Planck* resolution, we obtained the offsets of each *Herschel* image by a comparison with the derived intensity maps (Bernard et al. 2010). They were found to be 23, 320, 146, 59.8, and 18.7 MJy sr^{-1} at 70, 160, 250, 350, and 500 μm, respectively.

We used prepobs from getsf to reproject the *Herschel* images to the same size and number of pixels (3″, 2820 × 4050) and the hires method (Men'shchikov 2021a) to compute the temperature and surface density images at the *Herschel* resolutions. An advantage of the hires algorithm over other similar methods is that it can use the shortest-wavelength highest-resolution images, assuming that their emission is dominated by the normal dust grains in radiative equilibrium. Such high-resolution surface density images are helpful in our detailed study of the complex structural diversity in Vela C. The pixel-to-pixel SED fitting was performed by the fitfluxes utility (Men'shchikov 2016). The images at 160, 250, 350, and 500 μm were used to derive the temperature and surface density maps at 36.3″ resolution, the images at 160, 250, and 350 μm were used to obtain those maps at 24.9″ resolution, and the images at 160 and 250 μm were used to compute the maps at 18.2″ resolution. These three sets of temperatures and observed images (from 70 to 500 μm) were used to compute the surface density and temperature images (Fig. 1) with the improved resolutions of 5.9, 11.7, and 18.2″ (Men'shchikov 2021a). To reduce the noisiness of the 5.9″ surface densities induced by the *Herschel* 70 μm image, we smoothed the map to an 8.5″ resolution and used this in our work.

3.2. Source and filament extraction

We applied the multiscale multiwavelength extraction method getsf (Men'shchikov 2021a) to extract sources and filaments from the *Herschel* multiwavelength dust continuum images. The only constrained parameter that it requires is the maximum sizes of the structures to be extracted, determined from the observed images as the footprint radii of the largest source and widest filament (Sect. 3.1.3 in Men'shchikov 2021a). The footprint of a source or filament is defined as the full extent of the structures at zero (background) level (i.e., the area beyond which their contribution becomes negligible).
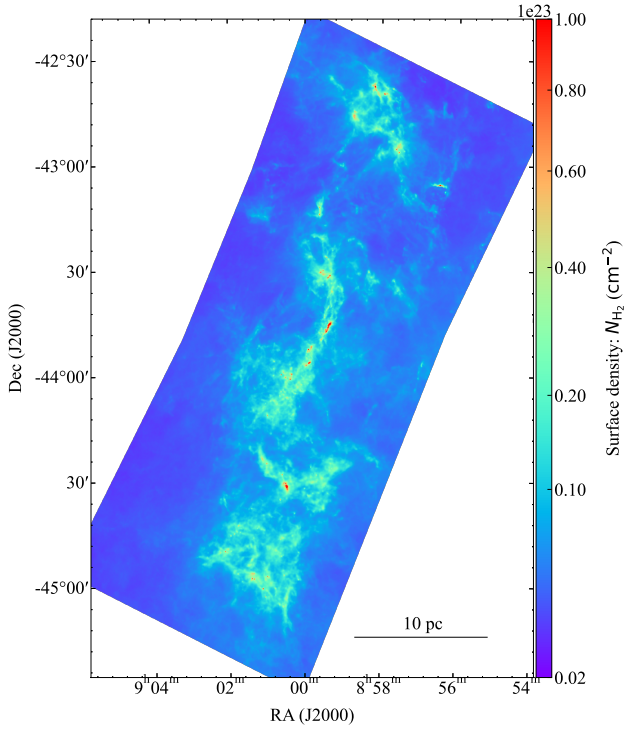
Fig. 1. High-resolution (11.7″) surface density map of Vela C, obtained from the *Herschel* images.

In our multiwavelength extraction of the sources and filaments with getsf in Vela C, we used the five *Herschel* images at 70–500 μm and three surface density images with the angular resolutions of 8.5, 11.7, and 18.2″. To extract sources the detection images combined information from all the images, whereas to extract filaments the 70 μm image was not used. After inspecting the images, we chose the following sets of maximum sizes: 40, 60, 80, 100, and 120″ for the *Herschel* wavebands and 25, 60, and 80″ for the surface densities.

3.3. Mass distribution in Vela C

Molecular clouds are complex structures that consist of various components (Bergin & Tafalla 2007). Sources are the round intensity peaks, corresponding to the individual fragments within molecular clouds. Filaments are the significantly elongated structures, often significantly curved, whose properties depend on the position along their crests. Both types of structure are characterized by a local overdensity and minimum in the gravitational potential of their parent cloud.

The hierarchical structure of Vela C (Figs. 1 and 2) includes the filamentary network, sources, and their backgrounds, all of them are separated from each other by getsf in the extraction process (Men'shchikov 2021a; Zhang et al. 2020). Assuming the cloud is optically thin at the observed wavelengths, the molecular cloud mass can be derived from its surface densities,

$$M_{\mathrm{C}} = \delta \mu_{\mathrm{H}_2} m_{\mathrm{H}} \sum_i \left(N_{\mathrm{H}_2} - N_{\mathrm{H}_2}^{\mathrm{b}} \right), \qquad (2)$$

where δ is the pixel area, $\mu_{\mathrm{H}_2} = 2.8$ the mean molecular weight per hydrogen molecule, m_{H} the mass of the hydrogen atom, $N_{\mathrm{H}_2}^{\mathrm{b}}$ the global background of the image, and the summation is done over all pixels. In Eq. (2), we adopted the value

$N_{\mathrm{H}_2}^{\mathrm{b}} = 2 \times 10^{21}$ cm^{-2} as the image background, corresponding to an integrated mass of $3.7 \times 10^4\ M_{\odot}$.

Comparisons with a simulated star-forming region (Fig. A.1 in Men'shchikov 2021a) suggest that the highest-resolution surface densities are expected to be more accurate for the structural components than the standard maps at a 36.3″ resolution. One exception is the unresolved protostellar peaks (which can be strongly overestimated because of the steep temperature gradients in the protostellar cores) created by the accretion luminosity. To give a sense of possible uncertainties in the derived masses of the structural components, Table 1 presents the estimates obtained from the surface densities at each of the three angular resolutions used in the extraction, along with the total masses at the lower resolutions. The bulk of the cloud is the low-density background with $N_{\mathrm{H}_2} \lesssim 5 \times 10^{21}$ cm^{-2}, accounting for 60% of the total mass M_{C}, whereas the components of filaments and sources constitute 35 and 3% of M_{C}, respectively.

A surface density probability distribution function (PDF$_N$) is useful for obtaining insights into the physical processes acting in the molecular cloud (Vazquez-Semadeni 1994; Passot & Vázquez-Semadeni 1998; Federrath et al. 2008; Kainulainen et al. 2009, 2011; Tassis et al. 2010; Kritsuk et al. 2011; Ballesteros-Paredes et al. 2011). Figure 3 shows the PDF$_N$ of the Vela C surface densities at 11.7″ resolution. At high surface densities ($N_{\mathrm{H}_2} \gtrsim 7 \times 10^{21}$ cm^{-2}), PDF$_N$ can be well fitted by a power law: $\mathrm{d}N/\mathrm{d}\log N_{\mathrm{H}_2} \propto N_{\mathrm{H}_2}^{-2.8 \pm 0.1}$. Surface densities are convertible to visual extinction, assuming A_V (mag) $= 0.94 \times 10^{21} N_{\mathrm{H}_2}$ cm^{-2} (Bohlin et al. 1978). The high-density tail corresponds to $N_{\mathrm{H}_2} \gtrsim 7\ A_V$. The PDF$_N$ of the interstellar medium, and in particular of the molecular clouds, is also a rapidly decreasing function, unless a special arrangement of masses occurs. Most of the space in the molecular cloud is filled with a low-density background and only a small fraction of the dense structures, as can be inferred from the rapid decline in PDF$_N$ (Kainulainen et al. 2009).

3.4. Selection of reliable cores

After applying getsf for source extraction, we adopted its definition of sources (cf. Sects. 1 and 3.2.2 in Men'shchikov 2021a). The sources are the relatively round emission peaks that are significantly stronger than the local surrounding fluctuations (of background and noise), suggesting the presence of the physical objects in space that produced the observed emission. In total, 3711 sources were detected by getsf.

Only sources that were good enough were then selected by getsf at each wavelength λ, using the following conditions (Sect. 3.4.6 in Men'shchikov 2021a): (1) $\Xi_\lambda > 1$, where Ξ_λ is the monochromatic goodness (combining detection significance and signal-to-noise ratio); (2) $\Gamma_\lambda > 1$, where Γ_λ is the detection significance from monochromatic single scales; (3) $F_{\mathrm{P}\lambda}/\sigma_{\mathrm{P}\lambda} > 2$, where $F_{\mathrm{P}\lambda}$ is the peak intensity and $\sigma_{\mathrm{P}\lambda}$ the peak intensity error; (4) $F_{\mathrm{T}\lambda}/\sigma_{\mathrm{T}\lambda} > 2$, where $F_{\mathrm{T}\lambda}$ is the total flux and $\sigma_{\mathrm{T}\lambda}$ the total flux error; (5) $A_\lambda/B_\lambda < 2$, where A_λ and B_λ are the major and minor widths at half maximum; (6) $A_{\mathrm{F}\lambda}/A_\lambda > 1.15$, where $A_{\mathrm{F}\lambda}$ is the full major axis of the elliptical footprint of a source.

The above criteria clean up the extraction catalog, removing spurious detections and selecting for further analysis only reliable and well-measurable sources, as verified by Men'shchikov (2021b). Conditions (1)–(4) ensure that the detected source peaks are sufficiently strong to be distinguished from the background and noise fluctuations. Condition (5) ensures that sources are circular or elliptical, excluding too elongated structures that
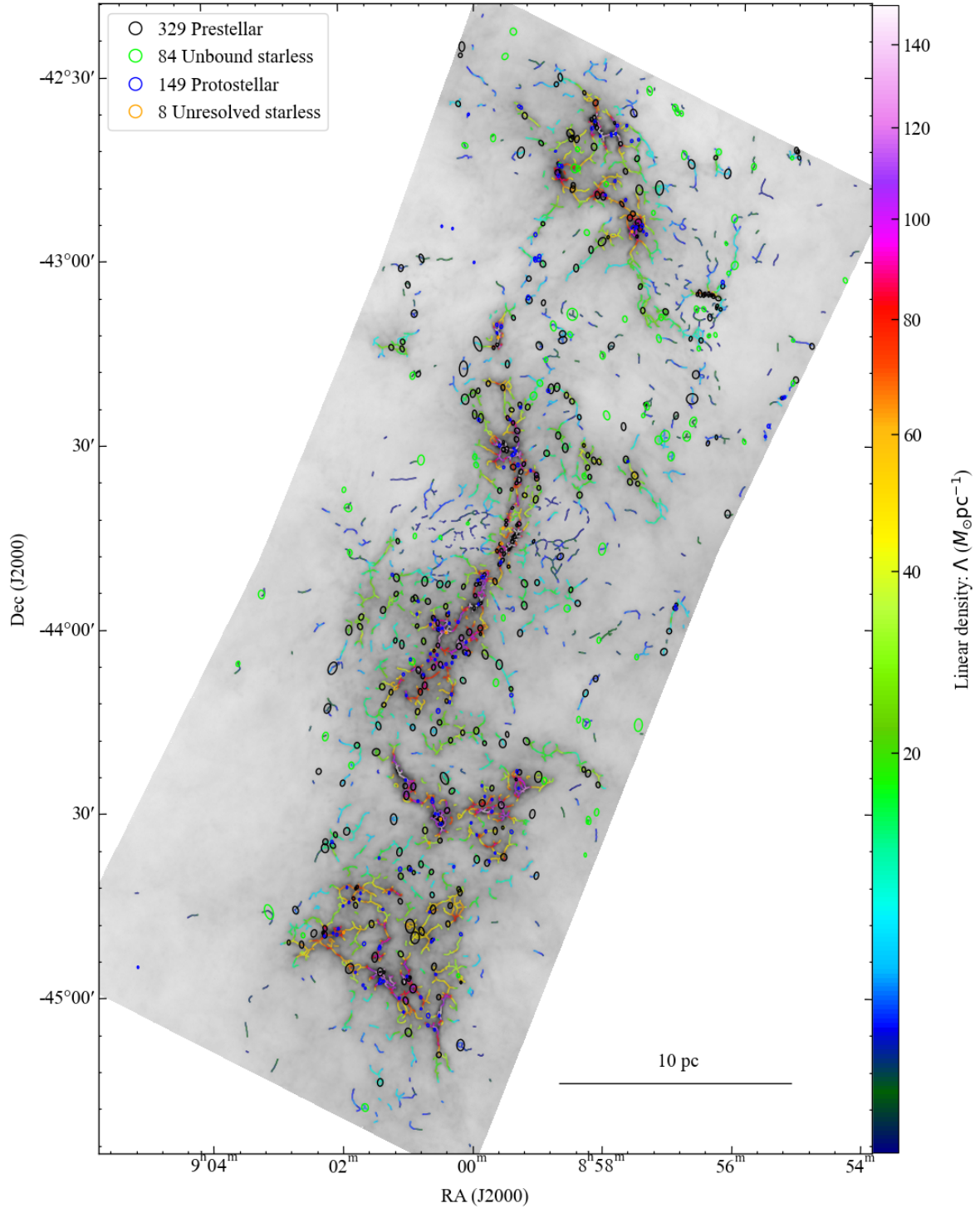
Fig. 2. Extracted cores and filaments in the Vela C molecular cloud on the 11.7″-resolution surface density image. The locations and sizes of the cores are measured from the surface density map. The black, green, and blue ellipses represent the 329 prestellar cores, 84 unbound starless cores, and 149 protostellar cores, respectively. The full axis of the ellipses is two times the Gaussian full width at half maximum (FWHM). Filamentary networks are shown by the global scale-independent skeletons of the filamentary structure. The filament linear density Λ^{W} in each point along the skeletons was estimated from Eq. (7) assuming a width of $W = 0.3$ pc (Fig. 11).

are unlikely to be sources. Condition (6) is used to discard the sources with unrealistically low ratios of their footprint to half maximum sizes. The criteria excluded a substantial number of detected peaks that are likely spurious and removed the sources with unreliable (inaccurate) measurements, leaving 1755 selected good sources.

Extragalactic sources are physically different from the starless cores or YSOs of our interest and must be excluded. Based on their peak positions, we cross-matched the sources with the SIMBAD database[2] (Wenger et al. 2000) and the NASA/IPAC

---

[2] https://simbad.cds.unistra.fr/simbad/

Table 1. Masses of the structural components of the Vela C molecular cloud, separated by getsf in the surface density images with different angular resolutions.

Resolution (″)	Sources M_{S} ($M_\odot$)	Filaments M_{F} ($M_\odot$)	Background M_{B} ($M_\odot$)	Total M_{C} ($M_\odot$)
8.5	6.3×10^3	3.0×10^4	5.3×10^4	9.0×10^4
11.7	2.2×10^3	2.5×10^4	4.6×10^4	7.3×10^4
18.2	2.4×10^3	2.6×10^4	4.4×10^4	7.2×10^4
24.9	–	–	–	7.2×10^4
36.3	–	–	–	7.2×10^4

Notes. The value of M_{S} at 8.5″ is likely significantly overestimated because it includes the protostellar sources with strong temperature gradients. The values of M_{B} and M_{C} are given after subtracting the global background $N_{\mathrm{H_2}}^{\mathrm{b}} = 2 \times 10^{21}$ cm^{-2} of the image (or $3.7 \times 10^4 \, M_\odot$), taken from the lower left corner of the image in Fig. 1.
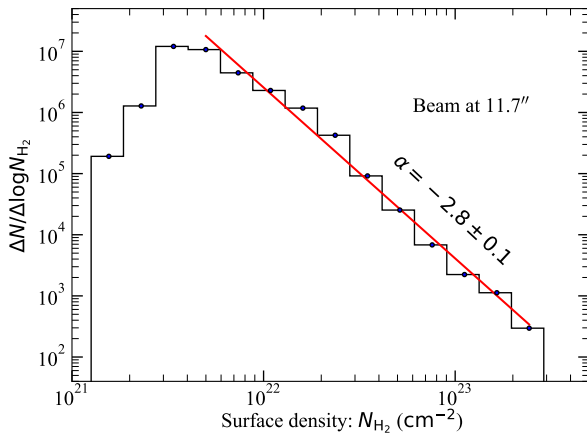

Fig. 3. Probability density function PDF$_N$ for Vela C. The vertical axis gives the actual number of pixels per bin in the 11.7″ resolution surface density image. At $N_{\mathrm{H_2}} \gtrsim 7 \times 10^{21}$ cm^{-2}, corresponding to $N_{\mathrm{H_2}} \gtrsim 7 \, A_V$, it can be fit well with a power law.

Extragalactic Database[3] (NED) within a 6″ radius. As a result, we removed one source based on SIMBAD and nine sources based on NED, which left us with 1745 acceptable sources.

Conditions (1)–(6) are necessary for a source to be acceptable in a single image or in a surface density map. In order to improve the reliability, we further selected as starless cores only those sources that are acceptable in at least two of the four wavebands of 160, 250, 350, and 500 μm and also in the surface density map at the 11.7″ resolution, but not detectable in the 70 μm map. Figure 4 illustrates the selection process that resulted in 421 acceptable starless cores.

The protostellar cores differ from the starless cores in that they produce accretion luminosity at their centers, which creates a strong unresolved peak at short wavelengths ($\lambda \lesssim 100$ μm), where the prestellar cores do not radiate a noticeable amount of energy. Following the standard approach, we identified as protostellar cores those sources that are detected and acceptable at 70 μm, not very resolved with a 5.9″ beam, and not too elongated, meaning that their major and minor half maximum sizes A and B obey the relations $(AB)^{1/2} < 1.5 \times 5.9''$ and $A/B < 1.3$. In addition, the protostellar cores must be acceptable in at least two of the four images at 160, 250, 350, and 500 μm and in the

---

[3] https://ned.ipac.caltech.edu

surface density image at 11.7″ resolution. Figure 5 illustrates the selection process that resulted in 149 acceptable protostellar cores.

3.5. Classification of extracted cores

Stars form in the process of the gravitational collapse of dense prestellar cores of a typical size of ∼0.1 pc that represent the local density maxima of the parent molecular cloud, producing the local minima of the gravitational potential (e.g., Bergin & Tafalla 2007; André et al. 2014; Zhang et al. 2020). Prestellar cores are the gravitationally bound starless cores with the potential to give birth to stars (Ward-Thompson et al. 2007; Bergin & Tafalla 2007; André et al. 2014; Könyves et al. 2015). The prestellar cores, supported by the pressure of the ambient gas of the parental cloud (e.g., Alves et al. 2001; Kirk et al. 2005), can be approximated by the equilibrium self-gravitational, isothermal Bonnor–Ebert (BE) spheres (Ebert 1955; Bonnor 1956). The BE model is useful even if the real core is not strictly isothermal or not in the hydrostatic equilibrium (e.g., Galli et al. 2002; Ballesteros-Paredes et al. 2003). The mass of the critical BE sphere can be expressed as (Bonnor 1956)

$$M_{\mathrm{BE}} \approx 2.4 \, R_{\mathrm{BE}} \, c_s^2 / G, \qquad (3)$$

where G is the gravitational constant, c_s the isothermal sound speed, and R_{BE} is the radius of the BE sphere, approximated in our work by the deconvolved radius,

$$R_{\mathrm{dec}} = (AB - O^2)^{1/2}, \qquad (4)$$

where A and B are the major and minor half maximum sizes, measured in the surface densities with the angular resolution of $O = 11.7''$. The sound speed in Eq. (3) was computed for the actual SED temperature T_{F} of each extracted core. Only the partially resolved and unresolved sources (resolvedness $(AB)^{1/2} O^{-1} > 1.1$) were used in Eq. (4) to avoid unacceptably large deconvolution errors (Men'shchikov 2023), and hence eight unresolved starless cores were ignored. The starless cores are deemed self-gravitating (bound) and classified as prestellar cores, when the ratio $\alpha_{\mathrm{BE}} = M_{\mathrm{BE}}/M_{\mathrm{core}} \leqslant 2$, where the core masses (and luminosities) are estimated by fitting the spectral energy distribution of the total fluxes F_λ of the sources over the *Herschel* wavebands. The resulting total number of prestellar cores is 329 and the number of the unbound starless cores is 84 (Fig. 2). The distributions of the source radii measured from the surface density maps at the angular resolutions of 8.5, 11.7, and 18.2″ are shown in Fig. 6.

Table A.1 presents a template of the online catalog of our multiwavelength source extraction and Table A.2 is a template of the online catalog of the derived parameters for the 570 reliable cores from Table A.1, which includes their dust temperatures T_{F}, masses M_{F}, and luminosities L_{F} (Fig. 7), obtained from fitting the spectral energy distribution (SED) of each core.

Figure 8 presents the mass-size diagram for the reliable cores in Vela C, where the deconvolved sizes were obtained from Eq. (4) using the measured sizes from the surface density image at 11.7″ resolution. The prestellar cores with $\alpha_{\mathrm{BE}} \leqslant 2$ are more massive than the starless cores not bound by gravity ($\alpha_{\mathrm{BE}} > 2$). Kauffmann et al. (2010) proposed an empirical formula $M \propto 870 \, M_\odot \, (R/\mathrm{pc})^{1.33}$ that provides a lower limit for the mass of massive stars that can form in molecular clouds, derived from observations of the distribution of masses of young stars in different environments. The presence of prestellar and protostellar cores above this line suggests that they likely form massive stars.
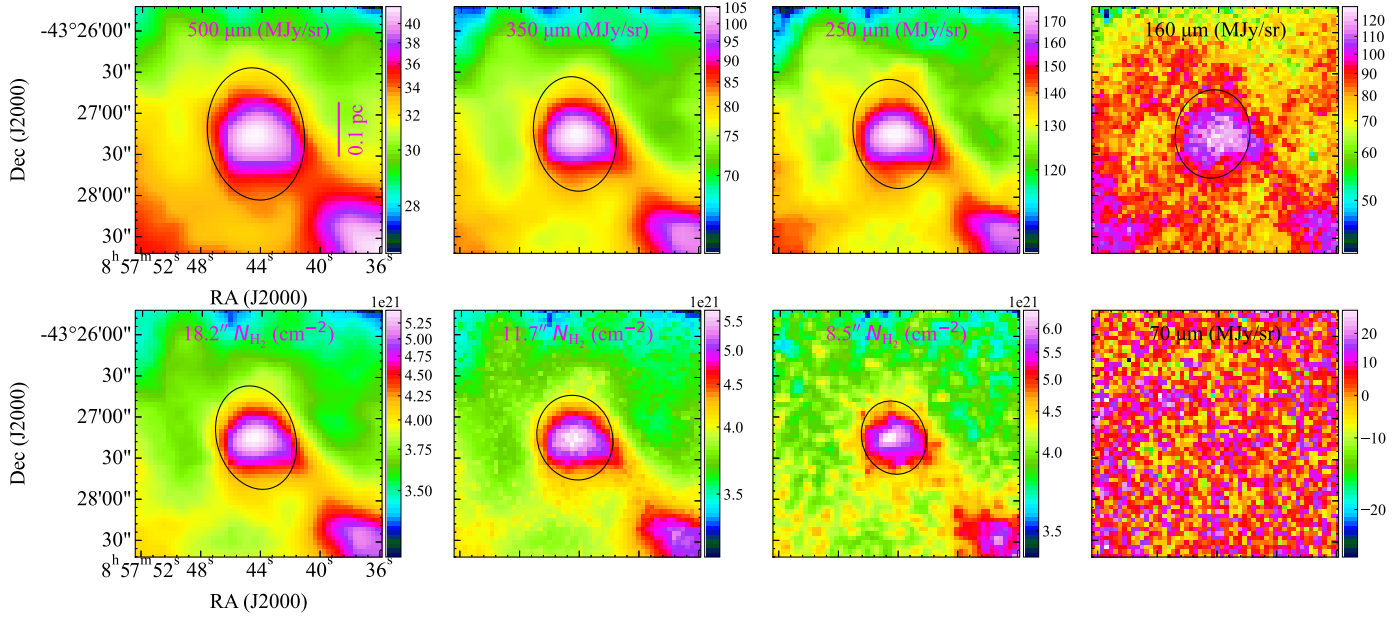
Fig. 4. Illustration of the selection criteria for starless cores in five *Herschel* images and in high-resolution surface density maps at resolutions of 8.5, 11.7, and 18.2″ (Sect. 3.4). The black ellipses represent the measured major and minor FWHM sizes.

Fig. 5. Illustration of the selection criteria for protostellar cores in five *Herschel* images and in high-resolution surface density maps at resolutions of 8.5, 11.7, and 18.2″ (Sect. 3.4). The black ellipses represent the measured major and minor FWHM sizes.
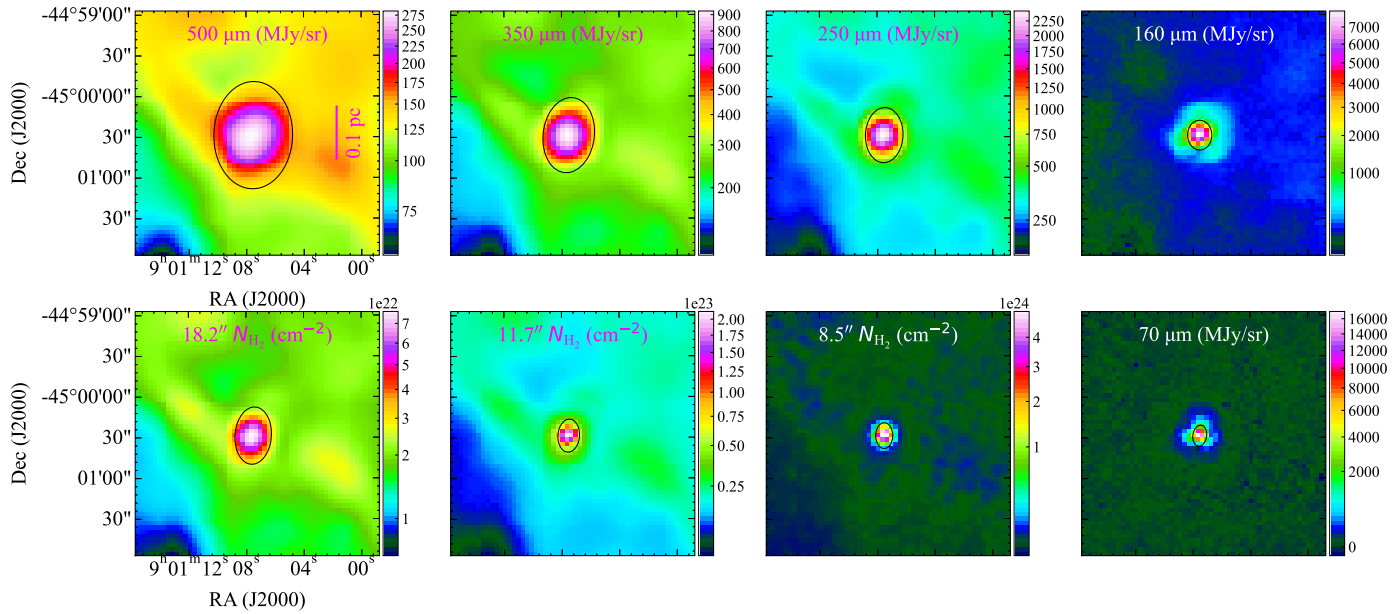
3.6. Core mass function

A fundamental property of molecular clouds is their mass distribution (Ballesteros-Paredes et al. 2020). Investigations of their CO emission (Sanders et al. 1985; Stutzki & Guesten 1990; Williams et al. 1994; Heyer & Terebey 1998; Kramer et al. 1998) and later studies of their dust continuum emission (Motte et al. 1998; Johnstone et al. 2000; Alves et al. 2007), have shown that the molecular clouds and their substructures do not have characteristic masses. Typically, they display a power-law distribution over mass:

$$\frac{\mathrm{d}N}{\mathrm{d}\log M} \propto M^{-\alpha}. \tag{5}$$

Using the masses derived from the SED fitting, we obtained the mass functions for the 421 starless, 329 prestellar cores, and 149 protostellar cores (Fig. 9). The CMFs for the starless and prestellar cores are indistinguishable at $M > 2\,M_\odot$ (all starless cores are bound) and they can be fitted well with $\mathrm{d}N/\mathrm{d}\log M \propto M^{-1.35\pm0.16}$ between 20 and 200 $M_\odot$. The power-law exponent is the same as that of the stellar IMF ($\alpha = 1.35$; Salpeter 1955). The CMFs also reveal that the population of protostellar cores has a deficit of massive cores with respect to the prestellar cores.

3.7. Physical properties of filaments

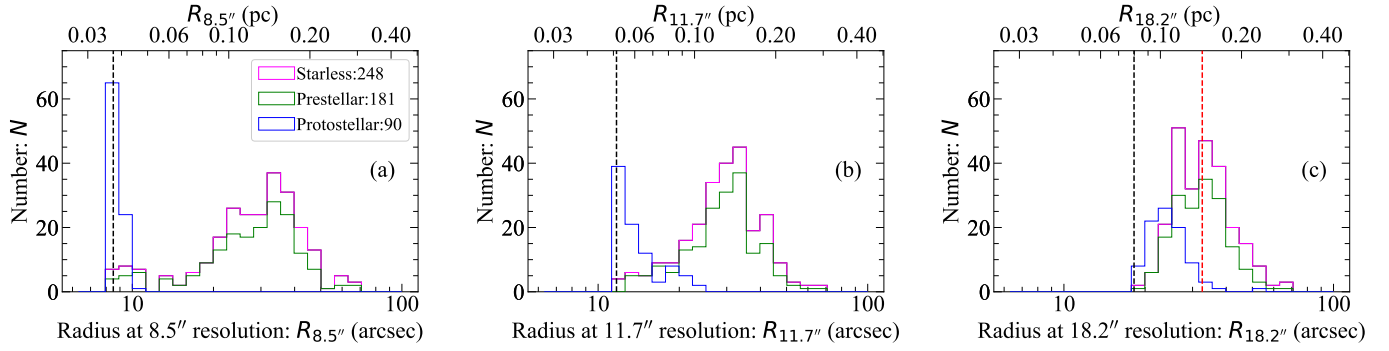Molecular filaments are the strongly elongated structures in molecular clouds (e.g., Men'shchikov et al. 2010;

Fig. 6. Histograms of the sizes of isolated cores, not blended with any other source in any waveband. The core radius is the arithmetic mean of the major and minor half maximum sizes, measured in the surface density images with three different resolutions (indicated by the vertical dashed lines). *Panel a*: distribution of source radii at 8.5″ resolution. *Panel b*: distribution of source radii at 11.7″ resolution. *Panel c*: distribution of source radii at 18.2″ resolution.
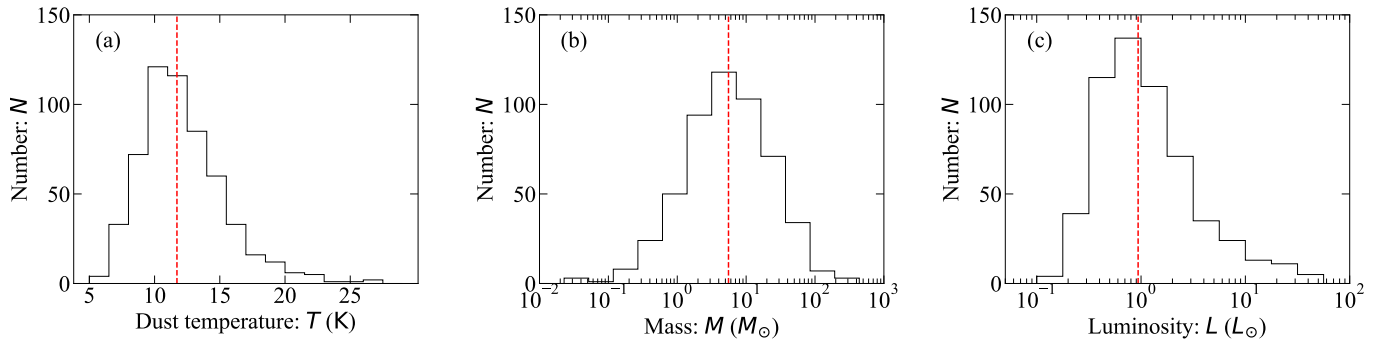

Fig. 7. Histograms of the physical parameters of the 570 reliable cores obtained from fitting SEDs of the extracted sources. *Panel a*: distribution of their average temperatures (median of 11.7 K). *Panel b*: distribution of their masses (median of 4.8 $M_\odot$). *Panel c*: distribution of their luminosities (median of 0.9 $L_\odot$). The red dashed lines indicate the median values.
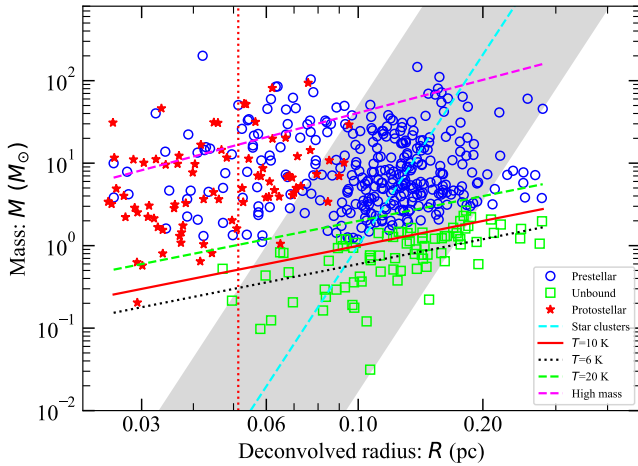

Fig. 8. Mass-size diagram for Vela C for the unbound cores (green squares), prestellar cores (blue circles), and protostellar cores (red stars). Only the partially resolved and resolved cores are shown (with sizes 10% larger than the 11.7″ beam) to ensure acceptably accurate deconvolution results using Eq. (4). The critical Bonnor-Ebert spheres with temperatures of 6, 10, and 20 K are displayed by the dashed black, dashed green, and solid red lines, respectively. The dashed cyan line is the radius-mass relation for open star clusters (Marks & Kroupa 2012, Eq. (7)) and the gray envelope represents its uncertainty range. The dashed magenta line indicates an empirical relationship proposed by Kauffmann et al. (2010). The physical scale of 0.05 pc at the 11.7″ resolution is indicated by the vertical line.
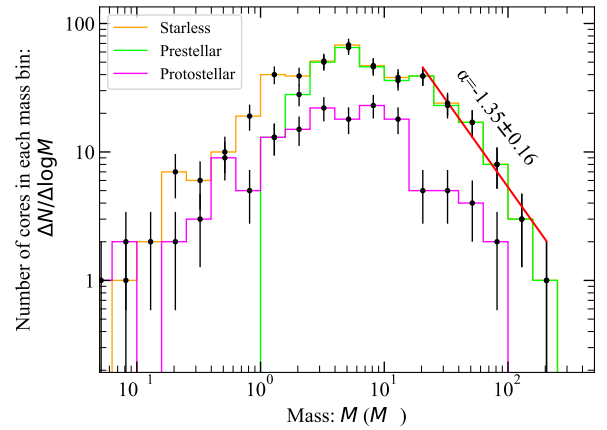
Fig. 9. Differential core mass function (dN/dlog$M$) for the 329 prestellar cores (green) 421 starless cores (orange), and 149 protostellar cores (magenta). The error bars correspond to the $\sqrt{N}$ statistical uncertainties.

André et al. 2014). The omnipresent filaments are usually blended with each other, and sources, and fluctuating background clouds, and the degree of blending becomes more severe at lower angular resolutions (Men'shchikov 2021a). Unfortunately, there are no reliable methods to accurately subtract backgrounds and deblend filaments from other structures in order to properly measure their physical parameters. Therefore,

Fig. 10. Illustration of a detected and measured filament in a high-resolution surface density image at 11.7″. *Left*: skeletons of the detected filaments with a contrast $C > 0.5$ is shown by the white curves and the black curve is the skeleton of a filament whose measured radial profile is shown in the right panel. *Right*: median one-sided surface density profiles measured on the two sides of the filament (blue and purple solid lines). The black dashed curve shows the beam profile. The median half maximum width of the filament is 0.33 ± 0.19 pc.
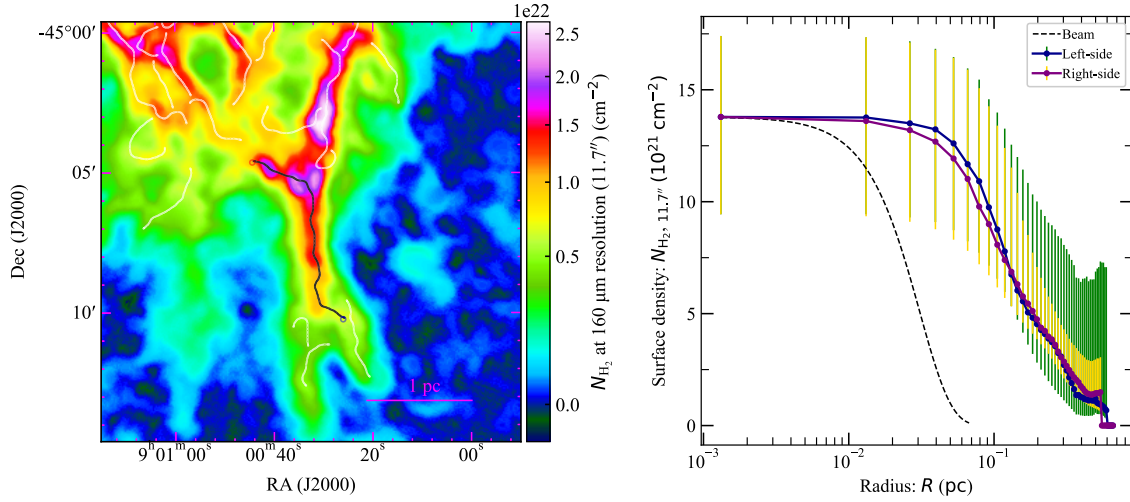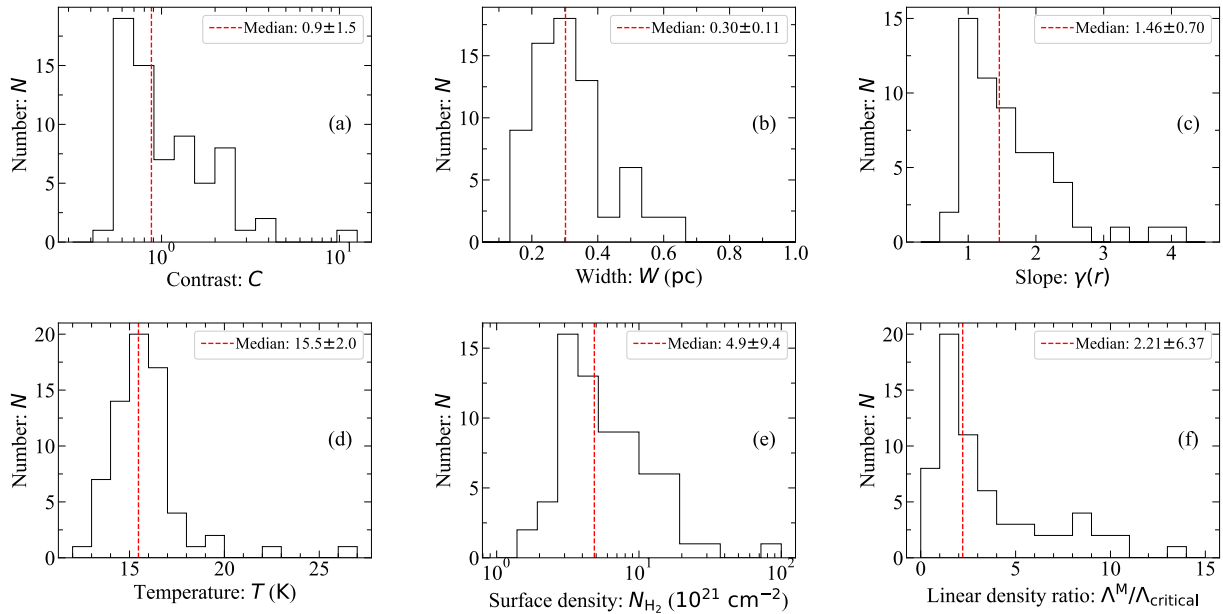

Fig. 11. Histograms of physical parameters of 68 selected filaments in Vela C. (*a*): filament contrasts; (*b*): filament widths; (*c*): logarithmic slope of profile; (*d*): dust temperatures along the filament crests; (*e*): surface densities along the crest; (*f*): ratio of linear density to the critical value. The red dashed line indicates the median value, and the error is the rms of the data.

it is preferable to choose clear examples of the isolated (not blended) relatively straight filaments on simple backgrounds, which would enable more accurate measurements of their properties and more reliable conclusions.

In practice, we used the simple (nonbranching) global skeletons, produced by getsf and measured the 11.7″-resolution surface densities of the component of filaments, separated from the sources and backgrounds. The contrast C of a source- and background-subtracted filament can be defined as

$$C = N_{H_2,F}/N_{H_2,B}, \tag{6}$$

where $N_{H_2,F}$ is the median value of the surface densities along the filament crest (skeleton) and $N_{H_2,B}$ the background surface density. After a visual inspection (Fig. 10), only the prominent

filaments with $C \gtrsim 0.5$ and length $L \gtrsim 0.4$ pc were used in the measurements of their profiles. We selected 68 filaments in which at least one side does not blend with the adjacent structures. A histogram of the physical parameters of the 68 selected filamentary filaments is shown in Fig. 11 and correlations of some parameters are displayed in Fig. 12.

We denote as W the median half maximum width of the surface density profiles of a filament along its length, and W_B the width measured on the broader side and W_N the width measured on the narrower side. When the two one-sided estimates are only moderately different (by less than 50%), we choose their arithmetic mean as the filament width W, otherwise we set the filament width $W = W_N$. The widths are in the range from 0.15 to 0.63 pc (median of 0.3 ± 0.11 pc) and they have no correlation with the filament temperature and surface density (Fig. 12). The
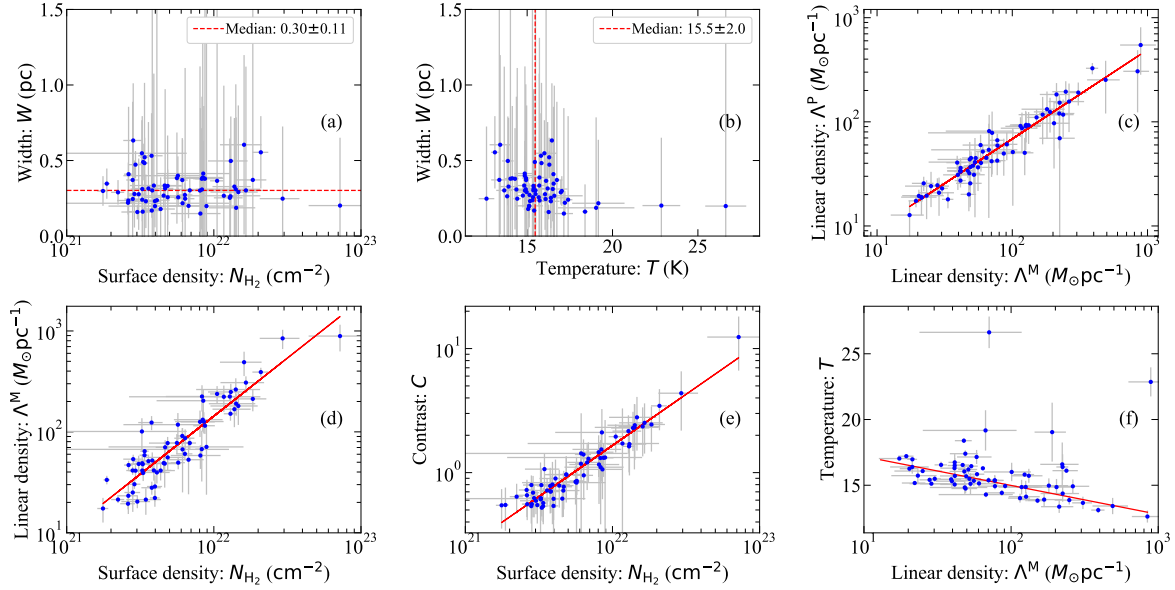
Fig. 12. Correlations of physical parameters of 68 filaments in Vela C. The red dashed lines indicate the median values and the red solid lines represent fits to the data: $\log \Lambda^P = 0.86 \log \Lambda^M + 0.13$ ($r = 0.96$), $\log \Lambda^M = 1.15 \log N_{H_2} - 23.16$ ($r = 0.91$), $\log C = 0.82 \log N_{H_2} - 17.92$ ($r = 0.95$), $T = -2.20 \log \Lambda^M + 19.38$ ($r = 0.77$), where r is the Pearson product moment correlation coefficient.

filament lengths L, defined as the length of the skeletons, are in the range from 0.35 to 2.14 pc (median of 0.7 pc). The median filament dust temperatures are in the range from 12.6 to 26.6 K (median of 15.5 K), measured on the crest in the temperature map.

Three estimates of the linear density Λ of each filament can be computed from the average integrated profile along the crest (Λ^P), from the average width (Λ^W), and from the filament mass (Λ^M):

$$\Lambda^P = \mu_{H_2} m_H \left\langle \int N_{H_2}(r, x) \, dr \right\rangle_x,$$
$$\Lambda^W = \mu_{H_2} m_H N_{H_2}^0 \langle W \rangle_x, \tag{7}$$
$$\Lambda^M = M_F / L.$$

Here the averaging is done over the coordinate x along the filament crest, $N_{H_2}^0$ is the crest surface density, and the filament mass M_F is obtained by integrating the surface densities over the filament footprint. The linear densities span more than an order of magnitude and are clearly correlated with some other parameters (Fig. 12). Table A.3 summarizes the derived physical parameters of the filaments that include their lengths, masses, linear densities, and widths.

With the assumption that filaments can be described by the infinitely-long linear isothermal hydrostatic nonmagnetic cylinders (Stodólkiewicz 1963; Ostriker 1964), their critical linear density has a very simple expression $\Lambda_{cr} = 2 c_s^2 / G$ that depends on the sound speed (gas temperature) in the filament. Observed filaments with linear densities above the critical value are usually considered unstable, fragmenting into cores under their own gravity (e.g., André et al. 2014; Zhang et al. 2020).

Applicability of the above instability criterion to the real observations is, however, completely unclear because the properties of the complex filaments observed with *Herschel* (e.g., Figs. 1, 2, and 10) show that the assumptions of the highly idealized model are invalid. The filaments do not resemble a linear cylinder, they are finite in length (actually relatively short) and nonisothermal, they have nonnegligible magnetic fields, and

there is no clear indication that they are in a hydrostatic equilibrium. The observed filamentary structures appear embedded in very complex, inhomogeneous environments (backgrounds), they are quite substantially curved, overlap with other nearby structures (filaments and sources), and have temperature gradients toward their centers as well as significantly variable radial profiles and widths (hence linear densities) along their crests (e.g., Figs. 6, 13, 19–23 in Men'shchikov 2021a). It is quite reasonable to conclude, therefore, that the critical linear density Λ_{cr}, based on the simplistic model assumptions, must be considered only a rough (order-of-magnitude) indicator that perhaps they might be unstable.

In the absence of a more realistic criterion, we analyzed the linear densities of the extracted filaments in Vela C, calculating the critical linear density using the median value of the dust temperature along each filament crest and assuming that Λ_{cr} is uncertain within a factor of 3. The linear densities Λ^W are shown in Fig. 2 for each point along the crests of the entire network of the filamentary structures. A distribution of filaments over the stability parameter Λ^M / Λ_{cr} is also shown in Fig. 11. The peak of the distribution is contained within the uncertainties $0.33 < \Lambda^M / \Lambda_{cr} < 3$, which means that most of the filaments (39 of 68) may be both supercritical and subcritical. There is also a tail of 29 filaments with the parameter value above 3 that can definitely be considered supercritical, in which are found 94 prestellar cores, 83 protostellar cores, and only 1 unbound starless core. On the other hand, the filaments with the stability parameter above 1 contain 210 prestellar cores, 127 protostellar cores, and 8 unbound starless cores. In other words, taking into account the uncertainties, the supercritical filaments contain only prestellar and protostellar cores.

4. Discussion

4.1. Extracted sources at different resolutions

Insufficient angular resolutions are known to make extracted sources artificially wider and more massive (Louvet et al. 2021; Men'shchikov 2023), because of the heavier blending with the

structured backgrounds and incorporation of the background into the extracted source, caused by the errors in background determination. Convergence tests at lower angular resolutions might indicate whether a given resolution is sufficiently high to produce accurate measurements (Louvet et al. 2021). To check for possible resolution effects, we measured properties of the extracted cores in the available surface densities at the resolutions of 8.5, 11.7, and 18.2″, selecting only isolated sources for the distributions of source sizes in Fig. 6 to avoid the considerable inaccuracies associated with deblending overlapping sources.

The starless (prestellar) cores are consistently well resolved at all three resolutions (Fig. 4), whereas the protostellar cores appear partially resolved at 18.2″, and become progressively less resolved toward the highest 8.5″ resolution (Fig. 5). The differences are caused by the fact that the protostellar cores are the accreting envelopes around protostars, generating accretion luminosity that heats up the inner opaque area of the envelopes to $T \gtrsim 1000$ K at radii $\theta \ll 1''$ (cf. Fig. 3 in Men'shchikov 2016), making the compact hot zone appear as an unresolved peak at 70 μm and a weaker peak at 160 μm (Fig. 5). The strong temperature gradients around the unresolved protostellar peaks make their derived surface densities inaccurate, especially the highest-resolution images (Appendix A in Men'shchikov 2021a).

The significantly overestimated unresolved peaks of the protostellar cores in the 11.7 and 8.5″ resolution surface densities provide a likely explanation of why their size distributions in Fig. 6 become increasingly unresolved at higher resolutions. We note, however, that protostellar envelopes have power-law volume densities $\rho \propto r^{-2}$ (surface densities $\sigma \propto \theta^{-1}$), and therefore their sizes A must be proportional to the angular resolution O, if their outer boundaries are sufficiently distant ($O \ll \Theta$). Simple numerical convolutions with Gaussian kernels confirm that the surface density image of such a power-law structure obeys the relationship $A = 1.6 \times O$. The size distribution of protostellar cores in Fig. 6 in the 18.2″ resolution surface densities (much less affected by the inaccuracies of pixel SED fitting) is indeed centered at sizes of approximately $1.3 \times 18.2''$.

4.2. Star formation and the CMF

Our analysis of the source extraction in Vela C resulted in the massive CMF that peaks at $5\,M_\odot$ and extends to $200\,M_\odot$, with a slope of -1.35 ± 0.16 above $20\,M_\odot$, which happened to have the same value as that proposed by Salpeter (1955) for an initial mass function (IMF) of stars (from 0.4 to $10\,M_\odot$). The cores extracted in this work are much more massive than the low-mass stars analyzed in the more abundant studies of the nearby regions of low-mass star formation. We constructed mass functions for the starless, prestellar, and protostellar cores. The CMF of protostellar cores can have a more complex shape, with a peak or plateau at intermediate masses, and a steep drop-off at high masses. This occurs because the protostar formation process tends to concentrate mass in a smaller range of core masses, and can also be affected by feedback mechanisms from the newly formed protostar, such as outflows and radiation (McKee & Tan 2002; Bate et al. 2003; Enoch et al. 2008).

There is a debate in the literature of whether the IMF and CMF have the same distribution. Some observations from the ground-based single-aperture telescopes (e.g., Motte et al. 1998; Alves et al. 2007) and *Herschel* (e.g., Könyves et al. 2015) have shown that there are similar mass distributions in the CMF and IMF in star-forming regions. There are also cases within the Galaxy where the CMF and IMF are dissimilar (e.g.,

Li et al. 2007; Motte et al. 2018; Zhang et al. 2018). The similarity of the two is often interpreted as indicating that there may be a constant core-to-star conversion efficiency (Alves et al. 2007). A recent ALMA study of the MM2 and MM3 clouds in W43 (Pouteau et al. 2022) found an excess of high-mass cores and a significantly shallower CMF slope. There are also indications that the CMF peak may shift to the lower masses with increasing angular resolution of the images (Louvet et al. 2021).

The mechanisms of high-mass star formation are not very clear yet. One scenario is that the massive dense cores collapse gravitationally and form high-mass stars because of their larger mass reservoirs and stronger gravitational potentials (McKee & Tan 2003; Tan et al. 2014). Other scenarios include disk fragmentation, competitive accretion, and mergers of the lower-mass protostars (e.g., Bonnell et al. 2004; Bate 2009; Kruijssen et al. 2012). The similarity of the CMF and IMF slopes at the high-mass end may be suggestive of a possible link between the formation of high-mass stars and the formation of their progenitors, the dense cores. More studies are necessary to reach a reliable understanding of the CMFs and their relationship with the IMF, including independent source and filament extractions and re-evaluation of the existing dataset of the *Herschel* observations of low-mass and high-mass star-forming regions.

4.3. Filamentary structures

Herschel discovered widespread networks of filamentary structures within the molecular clouds (Men'shchikov et al. 2010), proposed as the key actors in the formation of stars (André et al. 2014). The dense cores, formed by the gravitational fragmentation of the supercritical filaments are thought to be the progenitors of the next generations of stars (e.g., Zhang et al. 2020).

The filamentary structures in Vela C have crest temperatures of 15.5 K with a dispersion of roughly 2 K (Fig. 11). Radial dust temperature profiles, created from the dust temperature map, reveal shapes similar to an inverted surface density profile (Zhang et al. 2020) wherever the filament does not contain a hot source. The higher the surface or linear densities, the lower the crest temperature (Fig. 12) because of the increased shielding from the interstellar radiation field (Arzoumanian et al. 2019). The very common filament pattern is a main filament or a ridge and a network of stripes or subfilaments (e.g., Kirk et al. 2013; Men'shchikov 2021a). To facilitate more accurate measurements, getsf separated all branches of the skeleton network. The length of the 68 well-shaped filaments is approximately 0.5 pc, which is comparable to the lengths of the 599 filaments measured by Arzoumanian et al. (2019). Filamentary structures are interconnected with various nearby branches, and variations along the crest introduce uncertainties in the width, mass, and profile measurements (Fig. 10).

Studies of the nearby molecular clouds observed with *Herschel* suggested that the widths of the filaments are independent of the surface density and have a typical values of ~0.1 pc (Arzoumanian et al. 2011, 2019). Whether such a typical width actually exists or whether it is also applicable to the high-mass star-forming regions is still debated (Panopoulou et al. 2022; André et al. 2022). The widths of the filamentary structures that we selected in this work range from 0.15 to 0.63 pc, with a median value of 0.3 ± 0.11 pc. The angular resolution of the surface density map (11.7″) corresponds to ~0.05 pc at the distance of 905 pc adopted for Vela C, which means that all the filaments appear resolved. The widths and linear masses of the filaments in our study are similar to those found in the Cygnus X

high-mass star-forming region, located at 1.4 kpc (Hennemann et al. 2012).

5. Conclusions

Using the hires algorithm to create high-resolution surface densities from the *Herschel* observations and the getsf method to extract sources and filaments (Men'shchikov 2021a), we detected the sources and filamentary structures in the Vela C molecular cloud and analyzed their physical properties. Our systematic study of the individual molecular cloud led to the following main results.

The PDF_N of the surface density map with a resolution of $11.7''$ shows a prominent power-law tail at $A_V \gtrsim 7$ mag with the power exponent of -2.8 ± 0.1. The steep power law indicates that a major part of the molecular cloud space is the low-density background, with the source and filamentary components comprising 40% of the mass of the entire cloud $(4.6 \times 10^4\,M_\odot)$.

We extracted 570 reliable sources that were classified as 176 protostellar cores and 394 starless cores, which were further interpreted as 291 self-gravitating prestellar cores and 103 unbound cores. The median values of the core masses and dust temperatures, estimated from fitting the SEDs are $4.8\,M_\odot$ and 11.7 K, respectively. The starless and prestellar CMF can be well fitted with $\mathrm{d}N/\mathrm{d}\log M \propto M^{-1.35\pm0.16}$ between 20 and $200\,M_\odot$, with an exponent identical to that of the Salpeter's IMF. The masses and radii of the star-forming Vela cores are in a broad agreement with the birth radii deduced for open stars clusters by Marks & Kroupa (2012), which suggests that the prestellar cores more massive than $100\,M_\odot$ analyzed in this paper may be forming embedded star clusters.

We measured isolated sources on the surface density maps with angular resolutions of 8.5, 11.7 and $18.2''$ and found that the prestellar and unbound starless cores are well resolved, especially at the highest resolutions. Their distributions are centered on a half maximum size of $30''$ (0.13 pc). The proportionality of the sizes of the protostellar cores to the angular resolution is likely caused by both overestimated peaks in the derived surface densities and the power-law radial density distribution of the collapsing envelopes.

We measured the 68 well-behaved isolated filaments with contrasts $C \gtrsim 0.5$ and lengths $L \gtrsim 0.4$ pc, extracted in the surface density map of Vela C at $11.7''$ resolution. The filament widths are in the range from 0.15 to 0.63 pc, with a median of 0.3 ± 0.11 pc. The filament instability criterion $\Lambda > \Lambda_{\mathrm{cr}}$, based on the critical surface density of the highly simplified model of an infinite isothermal hydrostatic cylinder, is considered in this work to be only a rough uncertain indicator. We analyzed the linear densities of the extracted filaments, assuming that the critical value is uncertain within a factor of 3.

A majority of the filaments (39) may be supercritical or subcritical, within the large uncertainties. Only 29 filaments (with $\Lambda^M > 3\,\Lambda_{\mathrm{cr}}$) may be definitely considered supercritical, in which we found 94 prestellar cores, 83 protostellar cores, and only 1 unbound starless core. Thus, the supercritical filaments contain only prestellar and protostellar cores. We found that 64% of the prestellar cores and 85% of the protostellar cores are associated with the filamentary structures of $\Lambda^M > \Lambda_{\mathrm{cr}}$, whereas only 1% of the unbound starless cores are located on such filaments. The observed close connection between the cores and filaments is consistent with the idea that dense filamentary structures provide the most favorable local environment for the formation of stars in molecular clouds.

References

Alves, J. F., Lada, C. J., & Lada, E. A. 2001, Nature, 409, 159
Alves, J., Lombardi, M., & Lada, C. J. 2007, A&A, 462, L17
Andre, P., Ward-Thompson, D., & Barsony, M. 2000, in Protostars and Planets IV, eds. V. Mannings, A. P. Boss, & S. S. Russell (Tucson: Univeristy of Arizona Press), 59
André, P., Men'shchikov, A., Bontemps, S., et al. 2010, A&A, 518, A102
André, P., Di Francesco, J., Ward-Thompson, D., et al. 2014, in Protostars and Planets VI, eds. H. Beuther, R. S. Klessen, C. P. Dullemond, & T. Henning (Tucson: Univeristy of Arizona Press), 27
André, P. J., Palmeirim, P., & Arzoumanian, D. 2022, A&A, 667, A1
Arzoumanian, D., André, P., Didelon, P., et al. 2011, A&A, 529, L6
Arzoumanian, D., André, P., Könyves, V., et al. 2019, A&A, 621, A42
Baba, D., Sato, S., Nagashima, C., et al. 2006, AJ, 132, 1692
Ballesteros-Paredes, J., Klessen, R. S., & Vázquez-Semadeni, E. 2003, ApJ, 592, 188
Ballesteros-Paredes, J., Vázquez-Semadeni, E., Gazol, A., et al. 2011, MNRAS, 416, 1436
Ballesteros-Paredes, J., André, P., Hennebelle, P., et al. 2020, Space Sci. Rev., 216, 76
Bate, M. R. 2009, MNRAS, 392, 590
Bate, M. R., Bonnell, I. A., & Bromm, V. 2003, MNRAS, 339, 577
Bergin, E. A., & Tafalla, M. 2007, ARA&A, 45, 339
Bernard, J. P., Paradis, D., Marshall, D. J., et al. 2010, A&A, 518, A88
Bohlin, R. C., Savage, B. D., & Drake, J. F. 1978, ApJ, 224, 132
Bonnell, I. A., Vine, S. G., & Bate, M. R. 2004, MNRAS, 349, 735
Bonnor, W. B. 1956, MNRAS, 116, 351
Chabrier, G. 2005, Astrophys. Space Sci. Lib., 327, 41
Ebert, R. 1955, ZAp, 37, 217
Enoch, M. L., Evans, Neal J., I., Sargent, A. I., et al. 2008, ApJ, 684, 1240
Federrath, C., Klessen, R. S., & Schmidt, W. 2008, ApJ, 688, L79
Gaia Collaboration (Brown, A. G. A., et al.) 2018, A&A, 616, A1
Galli, D., Walmsley, M., & Gonçalves, J. 2002, A&A, 394, 275
Giannini, T., Elia, D., Lorenzetti, D., et al. 2012, A&A, 539, A156
Griffin, M. J., Abergel, A., Abreu, A., et al. 2010, A&A, 518, A3
Hennemann, M., Motte, F., Schneider, N., et al. 2012, A&A, 543, A3
Heyer, M., & Dame, T. M. 2015, ARA&A, 53, 583
Heyer, M. H., & Terebey, S. 1998, ApJ, 502, 265
Hill, T., Motte, F., Didelon, P., et al. 2011, A&A, 533, A94
Johnstone, D., Wilson, C. D., Moriarty-Schieven, G., et al. 2000, ApJ, 545, 327
Kainulainen, J., Beuther, H., Henning, T., & Plume, R. 2009, A&A, 508, L35
Kainulainen, J., Beuther, H., Banerjee, R., Federrath, C., & Henning, T. 2011, A&A, 530, A64
Kauffmann, J., Pillai, T., Shetty, R., Myers, P. C., & Goodman, A. A. 2010, ApJ, 716, 433
Kirk, J. M., Ward-Thompson, D., & André, P. 2005, MNRAS, 360, 1506
Kirk, H., Myers, P. C., Bourke, T. L., et al. 2013, ApJ, 766, 115
Könyves, V., André, P., Men'shchikov, A., et al. 2015, A&A, 584, A91
Kramer, C., Stutzki, J., Rohrig, R., & Corneliussen, U. 1998, A&A, 329, 249
Kritsuk, A. G., Norman, M. L., & Wagner, R. 2011, ApJ, 727, L20
Kroupa, P. 2001, MNRAS, 322, 231
Kroupa, P., Weidner, C., Pflamm-Altenburg, J., et al. 2013, in Planets, Stars and Stellar Systems, Vol. 5: Galactic Structure and Stellar Populations, eds. T. D. Oswalt, & G. Gilmore (Dordrecht: Springer), 115
Kruijssen, J. M. D., Pelupessy, F. I., Lamers, H. J. G. L. M., et al. 2012, MNRAS, 421, 1927
Li, D., & Goldsmith, P. F. 2012, ApJ, 756, 12
Li, D., Velusamy, T., Goldsmith, P. F., & Langer, W. D. 2007, ApJ, 655, 351
Liseau, R., Lorenzetti, D., Nisini, B., Spinoglio, L., & Moneti, A. 1992, A&A, 265, 577
Lorenzetti, D., Spinoglio, L., & Liseau, R. 1993, A&A, 275, 489
Louvet, F., Hennebelle, P., Men'shchikov, A., et al. 2021, A&A, 653, A157
Marks, M., & Kroupa, P. 2012, A&A, 543, A8
Massi, F., Lorenzetti, D., & Giannini, T. 2003, A&A, 399, 147
Massi, F., Weiss, A., Elia, D., et al. 2019, A&A, 628, A110

May, J., Murphy, D. C., & Thaddeus, P. 1988, A&AS, 73, 51
McKee, C. F., & Tan, J. C. 2002, Nature, 416, 59
McKee, C. F., & Tan, J. C. 2003, ApJ, 585, 850
Men'shchikov, A. 2013, A&A, 560, A63
Men'shchikov, A. 2016, A&A, 593, A71
Men'shchikov, A. 2021a, A&A, 649, A89
Men'shchikov, A. 2021b, A&A, 654, A78
Men'shchikov, A. 2023, A&A, in press, https://doi.org/10.1051/0004-6361/202346152
Men'shchikov, A., André, P., Didelon, P., et al. 2010, A&A, 518, A103
Men'shchikov, A., André, P., Didelon, P., et al. 2012, A&A, 542, A81
Minier, V., Tremblin, P., Hill, T., et al. 2013, A&A, 550, A50
Molinari, S., Swinyard, B., Bally, J., et al. 2010, PASP, 122, 314
Molinari, S., Schisano, E., Faustini, F., et al. 2011, A&A, 530, A133
Motte, F., Andre, P., & Neri, R. 1998, A&A, 336, 150
Motte, F., Zavagno, A., Bontemps, S., et al. 2010, A&A, 518, A77
Motte, F., Nony, T., Louvet, F., et al. 2018, Nat. Astron., 2, 478
Murphy, D. C., & May, J. 1991, A&A, 247, 202
Netterfield, C. B., Ade, P. A. R., Bock, J. J., et al. 2009, ApJ, 707, 1824
Ostriker, J. 1964, ApJ, 140, 1056
Panopoulou, G. V., Clark, S. E., Hacar, A., et al. 2022, A&A, 657, L13
Passot, T., & Vázquez-Semadeni, E. 1998, Phys. Rev. E, 58, 4501
Piazzo, L., Calzoletti, L., Faustini, F., et al. 2015, MNRAS, 447, 1471
Planck Collaboration XI. 2014, A&A, 571, A11
Poglitsch, A., Waelkens, C., Geis, N., et al. 2010, A&A, 518, A2
Pouteau, Y., Motte, F., Nony, T., et al. 2022, A&A, 664, A26
Salpeter, E. E. 1955, ApJ, 121, 161
Sanders, D. B., Scoville, N. Z., & Solomon, P. M. 1985, ApJ, 289, 373
Schisano, E., Molinari, S., Elia, D., et al. 2020, MNRAS, 492, 5420
Sousbie, T. 2011, MNRAS, 414, 350
Stodólkiewicz, J. S. 1963, Acta Astron., 13, 30
Stutzki, J., & Guesten, R. 1990, ApJ, 356, 513
Tan, J. C., Beltrán, M. T., Caselli, P., et al. 2014, in Protostars and Planets VI, eds. H. Beuther, R. S. Klessen, C. P. Dullemond, & T. Henning (Tucson: Univeristy of Arizona Press), 149
Tassis, K., Christie, D. A., Urban, A., et al. 2010, MNRAS, 408, 1089
Vazquez-Semadeni, E. 1994, ApJ, 423, 681
Ward-Thompson, D., André, P., Crutcher, R., et al. 2007, in Protostars and Planets V, eds. B. Reipurth, D. Jewitt, & K. Keil (Tucson: Univeristy of Arizona Press), 33
Wenger, M., Ochsenbein, F., Egret, D., et al. 2000, A&As, 143, 9
Williams, J. P., de Geus, E. J., & Blitz, L. 1994, ApJ, 428, 693
Yamaguchi, N., Mizuno, N., Saito, H., et al. 1999, PASJ, 51, 775
Zhang, G.-Y., Xu, J.-L., Vasyunin, A. I., et al. 2018, A&A, 620, A163
Zhang, G.-Y., André, P., Men'shchikov, A., & Wang, K. 2020, A&A, 642, A76
Zhang, C., Zhang, G.-Y., Li, J.-Z., & Li, X.-M. 2022, Res. Astron. Astrophys., 22, 055012
Zucker, C., Speagle, J. S., Schlafly, E. F., et al. 2020, A&A, 633, A51

Appendix A: Catalogs of dense cores and filaments identified with *Herschel* in Vela C

Our extraction in the *Herschel* SPIRE and PACS images of the Vela C molecular cloud identified a total of 570 dense cores, including 421 starless cores and 149 protostellar cores. A template of our online catalog, listing the observed properties of the extracted *Herschel* cores, is given in Table A.1. A template of our online catalog of the derived properties for each core (e.g., physical radius, mass, SED dust temperature) is given in Table A.2. A template of our online catalog of the physical parameters of 68 filaments (e.g., lengths, masses, linear densities, widths) is given in Table A.3.

Table A.1. Catalog of 570 reliable cores identified in the multiwavelength *Herschel* maps of the Vela C molecular cloud (template; full catalog provided online).

n (1)	RA (J2000, °) (2)	Dec (J2000, °) (3)	f (4)	Γ (5)	Ξ (6)	Core type (7)	SIMBAD (8)
1	134.8590106	-43.4369271	1	7.831E+03	1.491E+06	protostellar	[MHL2007] G264.9032+01.6584 1
2	135.2813467	-45.0079501	0	5.121E+03	5.271E+05	protostellar	[MHL2007] G266.2856+00.8533 1 MSX6C G266.2856+00.8533
3	135.1585678	-43.9928924	0	4.561E+03	5.021E+05	protostellar	MSX6C G265.4642+01.4561 IRAS 08588-4347
⋮							

f_{70} (9)	Γ_{70} (10)	Ξ_{70} (11)	$F_{P,70}$ (Jy/beam) (12)	$\sigma_{P,70}$ (Jy/beam) (13)	$F_{T,70}$ (Jy) (14)	$\sigma_{T,70}$ (Jy) (15)	$F_{G,70}$ (Jy) (16)	$S_{Jy,70}$ (") (17)	A_{70} (") (18)	B_{70} (") (19)	$A_{M,70}$ (") (20)	$B_{M,70}$ (") (21)	$\omega_{M,70}$ (") (22)	ϕ_{70} (°) (23)	$A_{F,70}$ (") (24)	$B_{F,70}$ (") (25)
0	9.654E+02	2.549E+04	2.462E+01	8.177E-02	3.648E+01	1.323E-01	2.787E+01	1.170E-01	1.300E+01	1.191E+01	1.798E+01	1.670E+01	1.186E+02	-4.644E+00	5.931E+01	5.433E+01
0	1.297E+03	4.218E+04	3.095E+01	6.114E-02	3.737E+01	1.347E-01	3.128E+01	1.170E-01	1.263E+01	1.096E+01	1.829E+01	1.678E+01	8.827E+01	-6.158E+00	8.303E+01	7.205E+01
0	1.323E+03	2.972E+04	3.596E+01	1.203E-01	4.212E+01	1.491E-01	3.463E+01	1.170E-01	1.302E+01	1.052E+01	1.58E+01	1.273E+01	1.154E+02	-3.342E+00	4.839E+01	3.910E+01
⋮																

f_{160} (26)	Γ_{160} (27)	Ξ_{160} (28)	$F_{P,160}$ (Jy/beam) (29)	$\sigma_{P,160}$ (Jy/beam) (30)	$F_{T,160}$ (Jy) (31)	$\sigma_{T,160}$ (Jy) (32)	$F_{G,160}$ (Jy) (33)	$S_{Jy,160}$ (") (34)	A_{160} (") (35)	B_{160} (") (36)	$A_{M,160}$ (") (37)	$B_{M,160}$ (") (38)	$\omega_{M,160}$ (") (39)	ϕ_{160} (°) (40)	$A_{F,160}$ (") (41)	$B_{F,160}$ (") (42)
⋮																

f_{250} (43)	Γ_{250} (44)	Ξ_{250} (45)	$F_{P,250}$ (46)	$\sigma_{P,250}$ (47)	$F_{T,250}$ (48)	$\sigma_{T,250}$ (49)	$F_{G,250}$ (50)	$S_{Jy,250}$ (51)	A_{250} (52)	B_{250} (53)	$A_{M,250}$ (54)	$B_{M,250}$ (55)	$\omega_{M,250}$ (56)	ϕ_{250} (57)	$A_{F,250}$ (58)	$B_{F,250}$ (59)
⋮																

f_{350} (60)	Γ_{350} (61)	Ξ_{350} (62)	$F_{P,350}$ (63)	$\sigma_{P,350}$ (64)	$F_{T,350}$ (65)	$\sigma_{T,350}$ (66)	$F_{G,350}$ (67)	$S_{Jy,350}$ (68)	A_{350} (69)	B_{350} (70)	$A_{M,350}$ (71)	$B_{M,350}$ (72)	$\omega_{M,350}$ (73)	ϕ_{350} (74)	$A_{F,350}$ (75)	$B_{F,350}$ (76)
⋮																

f_{500} (77)	Γ_{500} (78)	Ξ_{500} (79)	$F_{P,500}$ (80)	$\sigma_{P,500}$ (81)	$F_{T,500}$ (82)	$\sigma_{T,500}$ (83)	$F_{G,500}$ (84)	$S_{Jy,500}$ (85)	A_{500} (86)	B_{500} (87)	$A_{M,500}$ (88)	$B_{M,500}$ (89)	$\omega_{M,500}$ (90)	ϕ_{500} (91)	$A_{F,500}$ (92)	$B_{F,500}$ (93)
⋮																

$f_{8.5"}$ (94)	$\Gamma_{8.5"}$ (95)	$\Xi_{8.5"}$ (96)	$F_{P,8.5"}$ (97)	$\sigma_{P,8.5"}$ (98)	$F_{T,8.5"}$ (99)	$\sigma_{T,8.5"}$ (100)	$F_{G,8.5"}$ (101)	$S_{Jy,8.5"}$ (102)	$A_{8.5"}$ (103)	$B_{8.5"}$ (104)	$A_{M,8.5"}$ (105)	$B_{M,8.5"}$ (106)	$\omega_{M,8.5"}$ (107)	$\phi_{8.5"}$ (108)	$A_{F,8.5"}$ (109)	$B_{F,8.5"}$ (110)
⋮																

$f_{11.7"}$ (111)	$\Gamma_{11.7"}$ (112)	$\Xi_{11.7"}$ (113)	$F_{P,11.7"}$ (cm⁻²) (114)	$\sigma_{P,11.7"}$ (cm^{-2}) (115)	$F_{T,11.7"}$ (cm^{-2}) (116)	$\sigma_{T,11.7"}$ (cm^{-2}) (117)	$F_{G,11.7"}$ ($M_\odot$) (118)	$S_{Jy,11.7"}$ (") (119)	$A_{11.7"}$ (") (120)	$B_{11.7"}$ (") (121)	$A_{M,11.7"}$ (") (122)	$B_{M,11.7"}$ (") (123)	$\omega_{M,11.7"}$ (") (124)	$\phi_{11.7"}$ (°) (125)	$A_{F,11.7"}$ (") (126)	$B_{F,11.7"}$ (") (127)
0	8.125E+02	2.715E+03	1.160E+25	3.324E+23	1.314E+25	2.745E+23	2.722E+00	3.256E-02	1.236E+01	1.108E+01	1.215E+01	1.155E+01	4.561E+01	-2.453E+00	2.926E+01	2.870E+01
0	1.444E+03	1.028E+04	2.898E+25	3.574E+23	3.871E+25	3.844E+23	6.537E+00	1.356E-01	1.228E+01	1.115E+01	1.470E+01	1.354E+01	1.597E+02	-3.166E+00	3.847E+01	3.704E+01
0	1.004E+03	5.867E+03	2.054E+25	3.203E+23	2.531E+25	2.705E+23	4.340E+00	2.042E-01	1.220E+01	1.122E+01	1.216E+01	1.147E+01	1.353E+02	-2.502E+00	3.003E+01	2.927E+01
⋮																

$f_{18.2"}$ (128)	$\Gamma_{18.2"}$ (129)	$\Xi_{18.2"}$ (130)	$F_{P,18.2"}$ (131)	$\sigma_{P,18.2"}$ (132)	$F_{T,18.2"}$ (133)	$\sigma_{T,18.2"}$ (134)	$F_{G,18.2"}$ (135)	$S_{Jy,18.2"}$ (136)	$A_{18.2"}$ (137)	$B_{18.2"}$ (138)	$A_{M,18.2"}$ (139)	$B_{M,18.2"}$ (140)	$\omega_{M,18.2"}$ (141)	$\phi_{18.2"}$ (142)	$A_{F,18.2"}$ (143)	$B_{F,18.2"}$ (144)
⋮																

Notes. Catalog entries are as follows: (1) Source running number; (2) and (3): Centroid equatorial coordinates; (4) Flag describing global properties over all wavelengths (global flag), 0: source is not blended with any other source in any waveband; 1: source's footprints intersect by more than 20% in at least one waveband; 2: source's footprint area contains at least one other source; 3: source is causing a larger source to be substructured; (5) Detection significance over all wavelengths; (6) Monochromatic goodness (combining detection significance and signal-to-noise ratio); (7) Core type: protostellar, prestellar, unbound starless, and unresolved starless; (8) SIMBAD infrared source counterparts within a radius of 6" from the centroid position of the *Herschel* source; (9), (26), (43), (60), (77), (94), (111), (128): Wavelength-dependent flag; (10), (27), (44), (61), (78), (95), (112), (129): Detection significance from monochromatic single scales; (11), (28), (45), (62), (79), (96), (113), (130): Monochromatic goodness (combining detection significance and signal-to-noise ratio); (12), (29), (46), (63), (80), (97), (114), (131): Peak intensity; (13), (30), (47), (64), (81), (98), (115), (132): Error of $F_{P,\lambda}$; (14), (31), (48), (65), (82), (99), (116), (133): Total flux; (15), (32), (49), (66), (83), (100), (117), (134): Error of $F_{T,\lambda}$; (16), (33), (50), (67), (84), (101), (118), (135): Gaussian flux; (17), (34), (51), (68), (85), (102), (119), (136): Characteristic size of sources; (18)–(19), (35)–(36), (52)–(53), (69)–(70), (86)–(87), (103)–(104), (120)–(121), (137)–(138): Major and minor sizes at half maximum of sources; (20)–(21), (37)–(38), (54)–(55), (71)–(72), (88)–(89), (105)–(106), (122)–(123), (139)–(140): Major and minor size from intensity moments of sources; (22), (39), (56), (73), (90), (107), (124), (141): Position angle; (23), (40), (57), (74), (91), (108), (125), (142): Footprint factor; (24)–(25), (41)–(42), (58)–(59), (75)–(76), (92)–(93), (109)–(110), (126)–(127), (143)–(144): Major and minor sizes at footprint axes of sources.

Table A.2. Derived properties of 570 reliable cores identified in the multiwavelength *Herschel* maps of the Vela C molecular cloud (template; full table provided online).

n	RA (J2000, °)	Dec (J2000, °)	T (K)	σ_T (K)	M ($M_\odot$)	σ_M ($M_\odot$)	L ($L_\odot$)	σ_L ($L_\odot$)	$R_{8.5''}$ ('')	$R_{11.7''}$ ('')	$R_{18.2''}$ ('')	Core type
(1)	(2)	(3)	(4)	(5)	(6)	(7)	(8)	(9)	(10)	(11)	(12)	(13)
1	134.8590106	-43.4369271	1.934E+01	1.126E+00	4.141E+00	1.852E+00	2.087E+01	5.903E+00	8.500E+00	1.170E+01	2.117E+01	protostellar
2	135.2813467	-45.0079501	1.668E+01	7.853E-01	8.763E+00	3.839E+00	1.817E+01	5.138E+00	9.202E+00	1.170E+01	2.003E+01	protostellar
3	135.1585678	-43.9928924	1.977E+01	1.208E+00	4.317E+00	1.944E+00	2.477E+01	7.007E+00	8.500E+00	1.170E+01	1.990E+01	protostellar
...	...											

Notes. Catalog entries are as follows: (1) Source running number; (2) and (3): Centroid equatorial coordinates; (4) Derived dust temperature from SED fitting; (5) Uncertainty of derived temperature; (6) Derived total mass (gas and dust) from SED fitting; (7) Uncertainty of derived total mass; (8) Derived bolometric luminosity from SED fitting; (9) Uncertainty of derived luminosity; (10), (11), (12): Geometrical average between the major and minor FWHM size measured at 8.5, 11.7, and 18.2'' resolution; (13) Core type: protostellar, prestellar, unbound starless, and unresolved starless.

Table A.3. Catalog of the 68 selected filaments identified in the multiwavelength *Herschel* maps of the Vela C molecular cloud (template, full catalog only provided online).

n	RA (J2000, °)	Dec (J2000, °)	W ('')	L (pc)	W (pc)	W_α (pc)	W_β (pc)	$\overline{W}$ (pc)	$\overline{W}_\alpha$ (pc)	$\overline{W}_\beta$ (pc)	$\varsigma_{\overline{W}}$ (pc)	$\varsigma_{\overline{W}_\alpha}$ (pc)	$\varsigma_{\overline{W}_\beta}$ (pc)	N_W	$\Omega_{\overline{W}}$	$\Omega_{\overline{W}_\alpha}$	$\Omega_{\overline{W}_\beta}$
(1)	(2)	(3)	(4)	(5)	(6)	(7)	(8)	(9)	(10)	(11)	(12)	(13)	(14)	(15)	(16)	(17)	(18)
1	135.1401131	-45.1953743	6.775E+01	5.432E-01	2.973E-01	2.487E-01	3.552E-01	7.143E-01	2.614E-01	1.952E+00	4.964E-01	4.875E-02	3.450E+00	56	1.439E+00	5.361E+00	5.658E-01
4	135.134641	-45.1181584	7.461E+01	2.014E+00	3.274E-01	3.245E-01	3.302E-01	4.593E-01	5.432E-01	3.883E-01	1.933E-01	6.344E-01	2.733E-01	195	2.376E+00	8.561E-01	1.421E+00
6	135.1244612	-45.051289	6.876E+01	1.685E+02	3.017E-01	2.848E-01	3.195E-01	6.570E-01	8.204E-01	5.261E-01	4.348E-01	1.126E+00	5.126E-01	165	1.511E+00	7.284E-01	1.026E+00
17	135.0980823	-44.9982407	1.124E+02	5.151E-01	4.932E-01	5.596E-01	4.347E-01	5.778E-01	7.804E-01	4.278E-01	1.828E-01	5.036E-01	8.486E-02	54	3.161E+00	1.550E+00	5.042E+00
...	...																

n	N_{H_2} (cm^{-2})	$\varsigma_{N_{H_2}}$ (cm^{-2})	Λ^P ($M_\odot$/pc)	Λ^P_α ($M_\odot$/pc)	Λ^P_β ($M_\odot$/pc)	Λ^M ($M_\odot$/pc)	Λ^M_α ($M_\odot$/pc)	Λ^M_β ($M_\odot$/pc)	M ($M_\odot$)	M_α ($M_\odot$)	M_β ($M_\odot$)	ς_{Λ^P} ($M_\odot$/pc)	Ω_{Λ^P}	T (K)	ς_T (K)	C	ς_C
(1)	(19)	(20)	(21)	(22)	(23)	(24)	(25)	(26)	(27)	(28)	(29)	(30)	(31)	(32)	(33)	(34)	(35)
1	3.815E+21	4.963E+20	3.226E+01	2.607E+01	3.598E+01	5.206E+01	2.578E+01	7.835E+01	2.828E+01	1.401E+01	4.256E+01	1.050E+01	3.073E+00	1.549E+01	7.833E-02	7.059E-01	2.329E-01
4	1.379E+22	3.999E+21	1.204E+02	1.127E+02	1.217E+02	1.677E+02	2.069E+02	1.285E+02	3.377E+02	4.167E+02	2.588E+02	5.638E+01	2.136E+00	1.391E+01	5.460E-01	2.291E+00	7.993E-01
6	1.652E+22	5.429E+21	1.976E+02	1.958E+02	1.861E+02	3.076E+02	3.227E+02	2.926E+02	5.185E+02	5.438E+02	4.931E+02	4.743E+01	4.167E+00	1.366E+01	4.703E-01	2.520E+00	1.096E+00
17	1.304E+22	3.913E+21	1.927E+02	2.048E+02	1.845E+02	2.486E+02	2.150E+02	2.821E+02	1.280E+02	1.108E+02	1.453E+02	5.081E+01	3.793E+01	1.387E+01	3.380E-01	1.698E+00	7.485E-01
...	...																

Notes. Filaments are measured on 11.7''-resolution surface density map. Catalog entries are as follows: (1) Filament number; (2) and (3): Equatorial coordinates of the middle position; (4) and (6): Median of filament's FWHM measured from both sides in radial direction (different units); (5): Filament (skeleton) length; (7) and (8): Median of filament's FWHM measured from the left and right side in radial direction; (9) and (11): Mean value of filament's FWHM measured from both sides in radial direction; (10), (11): Mean value of filament's FWHM measured from the left and right side in radial direction; (12), (13), (14): Standard deviation about $\overline{W}$, $\overline{W}_\alpha$ and $\overline{W}_\beta$; (15) Number of points used for $\overline{W}$ and $\overline{W}_\alpha$; (16) Signal-to-noise ratio of $\overline{W}/\varsigma_{\overline{W}}$; (17) and (18): Signal-to-noise ratio of $\overline{W}_\alpha/\varsigma_{\overline{W}_\alpha}$ and $\overline{W}_\beta/\varsigma_{\overline{W}_\beta}$; (19) Filament crest value of surface density (on skeleton); (20) Standard deviation about N_{H_2}; (21) Linear density of filaments measured from median integrated profile in radial direction; (22) and (23): Linear density of filaments measured from the left and right median integrated profile in radial direction; (24) Linear density of filaments measured from N_{H_2}; (25) and (26): Linear density of filaments measured from M_α/L and M_β/L; (27) Filament mass derived from both sides; (28) and (29): Filament mass derived from the left and right side; (30) Standard deviation about Λ^P; (31) Signal-to-noise ratio of $\Lambda^P/\varsigma_{\Lambda^P}$; (32) Filament crest value of temperature (on skeleton); (33) Standard deviation about T; (34) Filament crest value of contrast (on skeleton); (35) Standard deviation about C.